CsPbI₃ Nanocrystals Go with the Flow: From Formation Mechanism to Continuous Nanomanufacturing

Kameel Antami, Fazel Bateni, Mahdi Ramezani, Cory E. Hauke, Felix N. Castellano, and Milad Abolhasani*

Despite the groundbreaking advancements in the synthesis of inorganic lead halide perovskite (LHP) nanocrystals (NCs), stimulated from their intriguing size-, composition-, and morphology-dependent optical and optoelectronic properties, their formation mechanism through the hot-injection (HI) synthetic route is not well-understood. In this work, for the first time, in-flow HI synthesis of cesium lead iodide (CsPbI₃) NCs is introduced and a comprehensive understanding of the interdependent competing reaction parameters controlling the NC morphology (nanocube vs nanoplatelet) and properties is provided. Utilizing the developed flow synthesis strategy, a change in the CsPbI₃ NC formation mechanism at temperatures higher than 150 °C, resulting in different CsPbI₃ morphologies is revealed. Through comparison of the flow- versus flask-based synthesis, deficiencies of batch reactors in reproducible and scalable synthesis of CsPbI₃ NCs with fast formation kinetics are demonstrated. The developed modular flow chemistry route provides a new frontier for high-temperature studies of solution-processed LHP NCs and enables their consistent and reliable continuous nanomanufacturing for next-generation energy technologies.

1. Introduction

Inorganic lead halide perovskite (LHP) nanocrystals (NCs) have been studied extensively since their discovery in 2015.[1–4] This interesting class of materials has resulted in groundbreaking advancements in different applications ranging from photonic devices[5–11] to photocatalysis.[12,13] The vast literature around LHP NCs stems from the dynamic and complex nature of their synthesis and processing universe that consists of a multitude of tunable and interdependent parameters affecting the NC morphology and thereby their optical and optoelectronic properties. The LHP NC morphologies of interest in this

work are nanoplatelets (NPLs) and nanocubes (NCubes) of cesium lead iodide (CsPbI₃). CsPbI₃ NCs have exhibited intriguing properties and performances in photonic and optoelectronic devices. The first reported power conversion efficiency (PCE) of a CsPbI₃ NC-based solar cell exceeded 10%,[5] and it has been rapidly rising over the past 5 years, with recent PCEs exceeding 15%.[7,14–16] Despite their success in the field, CsPbI₃ NCs still suffer from phase instability and charge carrier problems.[6,7] It has recently been demonstrated that ligand management on the CsPbI₃ NC surfaces can mitigate their phase instability and the charge carrier issues.[6,7,17] The understanding of CsPbI₃ NC formation mechanism and their reliable and scalable production are vital for further advancements and adoption of these promising class of semiconducting NCs by energy technologies.

NCubes have been the most extensively studied morphology of LHP NCs,[2,3] which is evident from their significant progress and ubiquitous use. Interests in LHP NPLs have progressed at a slower rate due to the intrinsic instability of these NCs caused by their high surface-to-volume ratio, resulting in the increased difficulty of their post-processing and long-term stability. Despite these challenges, LHP NPLs have recently been demonstrated to possess larger exciton binding energies (improves exciton recombination)[3,18] and enhanced emission and absorption characteristics compared to NCubes.[3,18,19] Additionally, the 2D nature of NPLs makes them more suitable for optoelectronic device fabrication[3,20] due to their tendency for face-to-face stacking[18,21] and their preference for wide-side assembly on a substrate.[19,22,23]

Most reports regarding LHP NPLs have been focused on cesium lead bromide (CsPbBr₃),[18,24–31] followed by a post-synthesis halide exchange reaction to produce other halide compositions.[18,25] One-pot synthesis of CsPbI₃ NPLs has also been reported[20,31] using ultrasonication at room temperature[20] and hot-injection (HI) with the aid of an additive halide salt (tin iodide) to induce NPL formation.[31] However, no universal consensus exists pertaining to how the formation of both anisotropic (NPLs) and isotropic (NCubes) CsPbI₃ NC structures can occur in a given reaction condition.

Different hypotheses have been proposed to explain the factors/mechanisms that favor anisotropic versus isotropic growth

K. Antami, F. Bateni, M. Ramezani, M. Abolhasani
Department of Chemical and Biomolecular Engineering
North Carolina State University
Raleigh, NC 27695-7905, USA
E-mail: abolhasani@ncsu.edu
C. E. Hauke, F. N. Castellano
Department of Chemistry
North Carolina State University
Raleigh, NC 27695-8204, USA

of NPLs and NCubes, respectively. The generally accepted NC growth model[32,33] states that the nucleation and growth of NCs is governed by the balance of surface reaction rate and monomer diffusion to the surface. Riedinger et al.[34] expanded the conventional NC growth model by including volume, surface, and edge energies, and revealed that cadmium selenide growth was favored on the narrow facet (leading to the NPL formation). Riedinger et al. proposed that this model could be applied to $CsPbX_3$ (X = Cl, Br, and I) NCs. Bekenstein et al.[18] provided a different NPL growth mechanism in which the 2D growth of $CsPbBr_3$ NPLs is guided by soft templates where NPLs grow inside lamellar structures. However, the exact nature and origin of the lamellar structures was not elucidated. In a different study, Burlakov et al.[24] coupled Monte Carlo simulations with experimentation and found that the $CsPbBr_3$ NPL growth was dictated by the competition between monomer and ligand formation on the NC surface, that is controlled by the temperature and ligand binding energy. The common theme between all proposed hypotheses of LHP NPL formation mechanisms[24,26,28,29,31] is the competition of cesium ions (Cs^+) with oleylammonium ions for the A-site cation in the perovskite NC, where oleylammonium ions impede the growth on the crystalline plane they attach to, leading to the NPL morphology.

Despite the success in the field and wide range of applications in which $CsPbI_3$ NCs have been used,[6,10] the scientific community is lacking a comprehensive understanding of their formation mechanism. The expansive range of parameters affecting $CsPbI_3$ NC synthesis coupled with their fast formation kinetics and process-sensitive nature of their HI synthetic route, complicate their accurate fundamental and applied studies using conventional flask-based synthesis techniques—with uncontrollable and irreproducible heat and mass transfer rates, resulting in reaction vessel size-dependent NC variations (**Figure 1**). In response, we present a modular flow chemistry strategy to systematically investigate different high-temperature synthetic routes of $CsPbI_3$ NCs, including HI, pre-heating (PH), and heat-up (HU). The most widely adopted $CsPbI_3$ NC synthesis method is HI, where the lead iodide (PbI_2) precursor is heated to the desired reaction temperature and the Cs precursor is then injected into the pre-heated PbI_2 precursor at relatively lower temperatures. In the HU synthesis technique, both Cs and PbI_2 precursors are mixed at room temperature and then heated to the desired reaction temperature. HU is not favorable in batch reactors due to the slow heating rates. In the PH synthesis technique, both precursors are heated to the reaction temperature before injection. PH synthesis in batch reactors poses temperature control problems for the second precursor, where it is difficult to maintain the desired temperature of the injected precursor.

Microscale flow synthesis strategies provide: i) automated high-throughput experimentation and in situ NC diagnostic capability through optical spectroscopy, ii) enhanced heat and mass transfer rates that allow for the rapid heating of the flow reactor and precursor streams followed by the equally rapid thermal quenching of the product stream, thereby effectively terminating the reaction and subsequent NC growth, iii) ease of precursor formulation which facilitates the use of different precursor ratios, and iv) access to early reaction timescales (<1 s). These advantages facilitate the accurate fundamental studies of
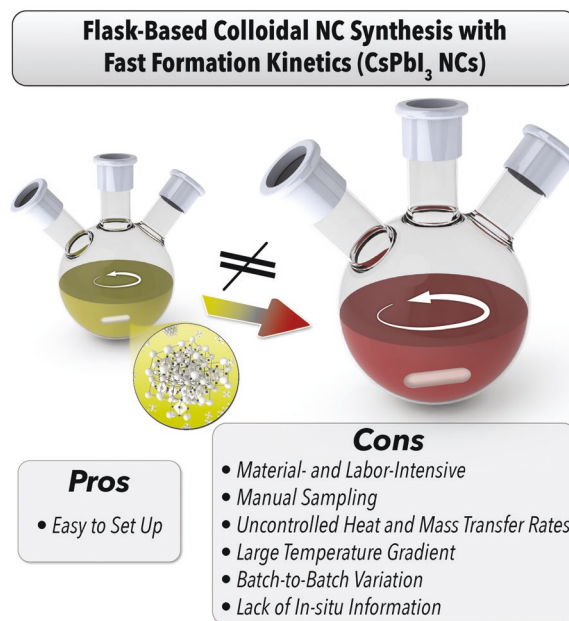

Figure 1. Overview of the advantages and challenges of conventional batch reactors for fundamental and applied studies of colloidal NCs with fast formation kinetics ($CsPbI_3$ NCs).

HI $CsPbI_3$ NC synthesis. Prior work of high-temperature flow synthesis of LHP NCs have mainly focused on their HU synthetic route,[35–38] where the precursors were mixed at room temperature followed by flowing into a heated reactor zone.[39]

In this work, utilizing a modular flow synthesis strategy, we study the formation mechanism and kinetics of $CsPbI_3$ NCs using the HI synthetic route. We map the chemical universe of the HI synthesis of $CsPbI_3$ NCs and provide a rationale for their isotropic versus anisotropic growth in a precisely controlled microreaction environment. We systematically examine the effect of key interrelated reaction parameters affecting the HI synthesis of $CsPbI_3$ NCs, including temperature, lead-to-cesium ratio (R_p), residence time (τ_r), and oleylammonium-to-Cs^+ ratio (R_{OC}), to unveil their formation mechanism and growth dynamics. We couple our in situ findings with offline transmission electron microscopy (TEM) imaging to provide a comprehensive understanding of the isotropic versus anisotropic growth of $CsPbI_3$ NCs and reveal a change in their formation mechanism as the synthesis temperature increases beyond 150 °C. Building on these findings, we demonstrate the role of flow reactors in the consistent large-scale synthesis of $CsPbI_3$ NCs with desired morphology and optical properties, without sacrificing the NC quality.

2. Results and Discussion

The modular flow reactor was specifically designed to mimic the HI synthetic route commonly used for the batch synthesis of $CsPbI_3$ NCs,[1] and at the same time allow for exploration of both HU and PH synthesis techniques. **Figure 2**A presents a schematic of the developed modular flow reactor for the high-temperature synthesis of $CsPbI_3$ NCs. Machined aluminum blocks
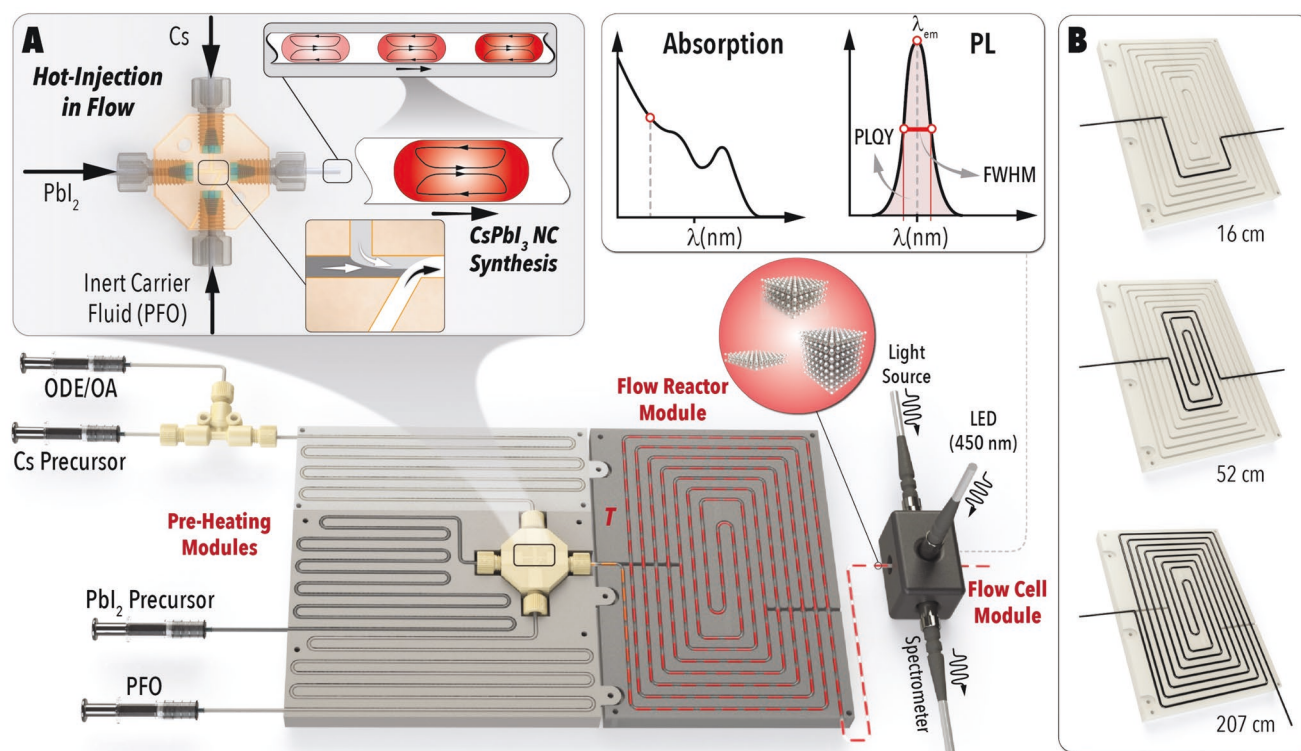
Figure 2. A) Schematic of the modular flow chemistry platform developed for the high-temperature synthesis of CsPbI$_3$ NCs. B) Illustration of three different flow reactor lengths (volumes) accommodated within the same heating module. The total flow rate used for this study was 1500 µL min^{-1} (PFO = 500 µL min^{-1}, PbI$_2$ precursor = 500 µL min^{-1}, and diluted Cs precursor = 500 µL min^{-1}).

(Protolabs) with serpentine flow reactor patterns were used to house and rapidly heat perfluoroalkoxy (PFA) tubing (outer diameter (OD): 1/16 in., inner diameter (ID): 0.02 in.). Cartridge heaters embedded into the machined aluminum plates (Watlow, diameter: 0.12 in., length: 4 in.), connected to a PID temperature controller (Omega, CN9311), were used for heating the PH and the flow reactor modules. The flow reactor section of the modular flow reactor, shown in Figure 2, is designed in a way to accommodate 36 different lengths (volumes) of the flow reactor within the same heating plate (Figure 2B), thereby removing the need for the redesign and machining of a new flow reactor module for each flow reactor volume. This unique feature is critical to ensure the precursor mixing dynamics of CsPbI$_3$ NCs remain the same at different reaction times (residence times) during the in-flow high-temperature synthesis (i.e., similar total flow rate for different flow reactor volumes), and do not impact the NC formation mechanisms and properties.

Using a separate heating module for each precursor allows for an on-demand configuration of the synthetic route (HI, PH, or HU) before entering the flow segmentation module (Figure 2A). An inert continuous phase (perfluorinated oil, PFO) is used for the flow segmentation and is heated to the desired reaction temperature for HI and PH synthesis of CsPbI$_3$ NCs. The use of PFO serves two purposes: i) it is used as a carrier phase to segment the reactive phase and induce an axisymmetric swirling pattern within the formed droplets to enhance mixing, and ii) it preferentially wets the PFA inner wall and forms a lubrication film to isolate the reactive droplets and prevent fouling.[4,40–42] The Cs precursor stream is mixed with an octadecene (ODE)/oleic acid (OA) solvent stream at the room temperature, using a T-junction (IDEX Health and Sciences), before entering the flow segmentation module to achieve the desired Cs concentration (Figure 2A). The segmentation module is a custom-machined four-way junction (polyether ether ketone), specifically designed to achieve reliable and uniform flow segmentation with two reactive streams and a carrier fluid.[43,44] The volumetric injection ratio of the Cs and PbI$_2$ precursors used in this study is 1:1 to achieve a wider range of in-flow tuning of the Cs concentration to explore different R_p values. Following the injection of the Cs precursor into the PbI$_2$ stream within the segmentation module, the formed two-phase flow enters the heated flow reactor module (red and dark gray tubing in Figure 2A) for the desired residence time. In order to maintain identical precursor mixing timescales within the reactive phase droplets, the residence time was varied by changing the flow reactor length placed inside the same flow reactor heating module (Figure 2B). An additional length of the flow reactor tubing (2 m long) was included past the heating module to ensure that the reaction product reaches room temperature before entering the in situ spectral characterization module.

The spectral characterization module is a custom-designed three-port flow cell connected to the outlet of the flow reactor. The flow cell is a machined aluminum block with three optical fiber (Ocean Insight, 600 µm diameter) ports and a fluorinated ethylene propylene tubing (OD: 1/16 in., ID: 0.03 in.).[40] The flow cell allows for real-time spectral characterization of the in-flow synthesized CsPbI$_3$ NCs through UV–vis absorption and photoluminescence (PL) spectroscopy (Figure 2A). The optical

fibers are connected to a broadband light source (Ocean Insight, DH-2000-BAL) for UV–vis absorption spectroscopy, a 450 nm light emitting diode (Thorlabs) as the PL excitation source, and a miniature fiber-coupled spectrometer (Ocean Insight, HDX). In situ PL spectroscopy is used to monitor the peak emission wavelength, λ_{em}, and calculate the relative PL quantum yield (PLQY) of the in-flow synthesized $CsPbI_3$ NCs.

The quantum-confined nature of $CsPbI_3$ NCs implies that a change in the NC size or shape would correspond to a change in λ_{em}, where smaller dimensions (i.e., smaller NCubes or thinner NPs) cause a blue-shifted λ_{em}, provided one (NPLs) or three (NCubes) NC dimensions are smaller than the Bohr radius.[1,45] The location of the first excitonic peak of the in situ obtained UV–vis absorption spectra is indicative of the size/shape of the NCs, where smaller/thinner NCs cause a blue-shift. The absorption intensity at high photon energies is directly correlated to the concentration of the synthesized NCs, using the Beer–Lambert law, which enables monitoring of the reaction progress and is also used for relative PLQY calculations.

One of the important factors in multi-phase flow synthesis of colloidal NCs is the uniformity of the droplet size (related to mixing time) and velocity (related to residence time) within the train of droplets flowing along the flow reactor at high reaction temperatures. In the first set of experiments, we studied the multi-phase flow uniformity within the modular flow reactor shown in Figure 2A. The light absorption difference between the reactive and the carrier phase flowing in the flow cell is utilized to automatically identify the boundaries of each respective fluid.[40] Figure S1, Supporting Information shows a PL intensity time-series plot at 450 nm for different reaction temperatures and illustrates the droplet uniformity of the multi-phase flow format employed for synthesizing $CsPbI_3$ NCs at different reaction temperatures.

One of the unique attributes of automated flow reactors integrated with in situ characterization modules is access to early reaction timescales (<1 s) with a time resolution that is impossible to attain in batch reactors. Furthermore, when synthesizing NCs in batch reactors, there is a considerable time delay between the precursor injection and transfer of the reaction vessel into an ice bath which limits the lower bound of the feasible reaction time in flask-based synthesis techniques (≈5 s). Additionally, flask-based colloidal NC synthesis methods suffer from comparatively lower heat transfer rates than flow reactor, which results in a temperature gradient across the flask where the outer edge cools at a rate faster than the core of the vessel where NC growth continues to happen. In contrast, the reaction product cools significantly faster and more uniformly in flow reactors compared to batch, due to the reduced active fluid volume, resulting in rapid thermal quenching of the NC growth after the reaction at high temperatures. Based on a 2D numerical heat transfer simulation of the flow reactor used in this work (see Figure S2, Supporting Information), the reaction product cools at a rate of 400 °C s^{-1} (0.4 s to cool down from 180 to 20 °C).

The plug-and-play and modular nature of the developed flow chemistry strategy allows for facile exploration of all three high-temperature synthetic routes of $CsPbI_3$ NCs (HI, PH, and HU), while maintaining a precise control over the enhanced heat and mass transfer rates. **Figure 3** presents the three different configurations of the modular flow chemistry platform utilized for the in-flow synthesis of $CsPbI_3$ NCs using the HI, PH, and HU synthetic routes. It should be noted that the only difference between the three configurations of the flow chemistry platform for different high-temperature synthetic routes is the number of precursor heating modules that can be readily inserted (or removed) to switch between HU, HI, and PH synthesis techniques.

The UV–vis absorption and PL spectra as well as the TEM images of the in-flow synthesized $CsPbI_3$ NCs using the HI, PH, and HU synthetic routes using the same starting precursors, reaction temperature, and residence time are presented in Figure 3. The results shown in Figure 3 illustrate that the HU synthesis technique resulted in the NC population with the highest polydispersity, while the HI and PH techniques exhibited a similar uniform NC size distribution, peak emission wavelength, FWHM, and PLQY (Figure 3, inset). Analysis of the selected area electron diffraction rings of the in-flow synthesized $CsPbI_3$ NCs revealed that all three synthetic routes resulted in NCs with an orthorhombic crystalline phase (Figure S3, Table S1, Supporting Information). However, the energy dispersive spectroscopy analysis of the $CsPbI_3$ NCs revealed a sub-stoichiometric perovskite structure for the NCs synthesized using the HU synthesis technique (Note S3, Supporting Information). Based on these findings, we selected the in-flow HI configuration of the modular flow reactor as the synthetic route for the systematic studies of $CsPbI_3$ NC formation mechanism due to its higher NC quality than the HU synthesis technique and lower energy demand than the PH synthesis technique (2 heating modules for the HI vs 3 for the PH).

Following the characterization of the developed fluidic NC synthesizer, we utilized the modular flow reactor to systematically investigate the formation mechanism and kinetics of HI synthesis of $CsPbI_3$ NCs. **Figure 4** shows a summary of the in situ obtained UV–vis absorption and PL spectra of the in-flow HI synthesis of $CsPbI_3$ NCs for reaction temperatures from 130 to 180 °C at different τ_r and R_p (see Figure S4, Supporting Information for 110 °C). The first notable observation from Figure 4 is that decreasing R_p (i.e., increasing Cs$^+$) results in red-shifted first excitonic peaks (absorption spectra) and emission wavelength (PL), indicative of the increased NC growth, where higher energy peaks (i.e., absorption peaks at ≈550 and 600 nm, PL peaks at ≈600 and 623 nm) represent either NPLs or small NCubes. Second, an increase in the reaction temperature and τ_r also leads to the increased NC growth. However, increasing the reaction time to 16 s results in a decrease of the UV–vis absorption intensity which can be attributed to the defocusing of the NC population due to ripening.[46]

The multimodal nature of the PL spectra of the in-flow synthesized $CsPbI_3$ NCs at lower R_p values (Figure 4; Figure S4, Supporting Information) implies the presence of different NC populations in the reaction mixture. The PL peak positions of 600, 623, and 685 nm (Figure 4; Figure S4, Supporting Information) are in agreement with the results reported by Tong et al.,[20] attributing them to $CsPbI_3$ NPLs with monolayer thicknesses of 3, 4, and 16 layers, respectively. However, due to the different synthetic routes in which NPLs reported by Tong et al. were synthesized (room temperature ultrasonication vs HI reported in this work) and considering that small NCubes
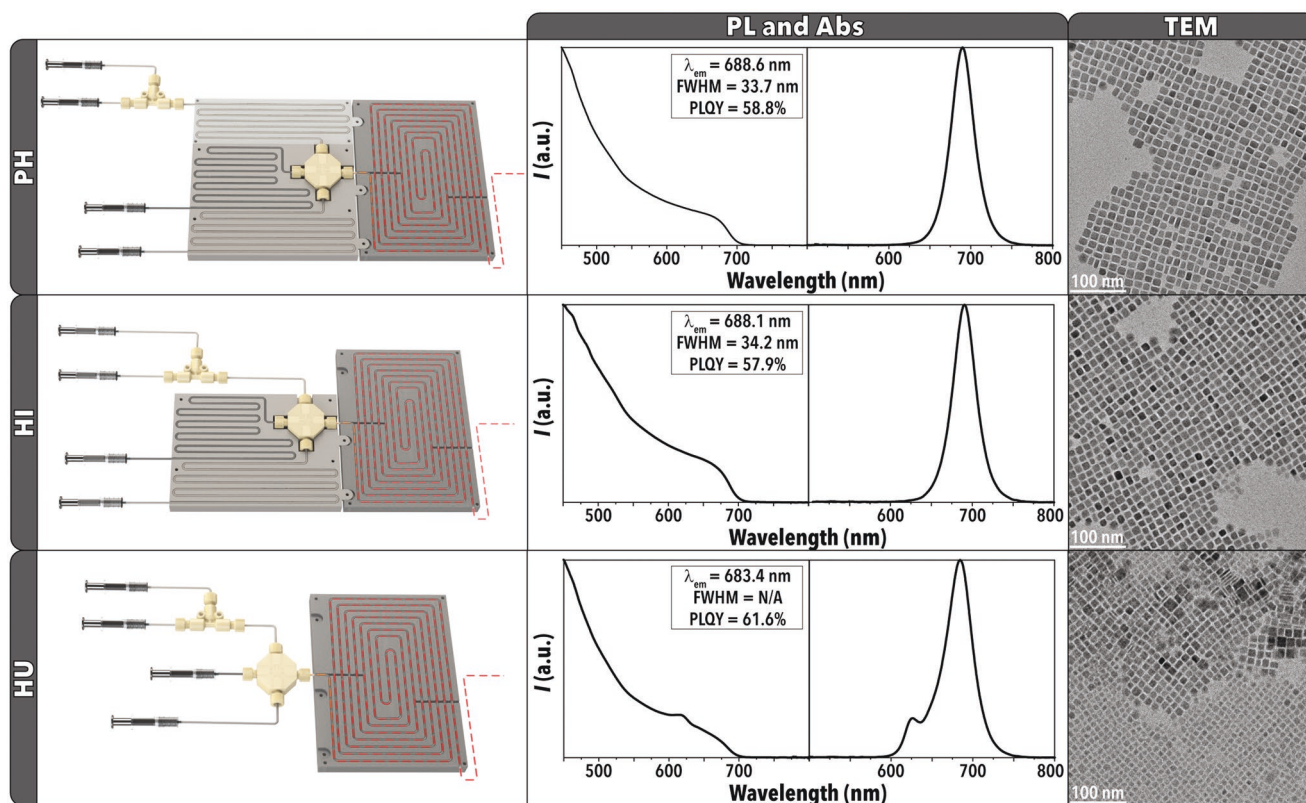
Figure 3. A schematic illustration of the three configurations of the modular flow chemistry platform for high-temperature synthesis of CsPbI$_3$ NCs (left). The UV–vis absorption and photoluminescence spectra of the in-flow synthesized CsPbI$_3$ NCs using the same reaction conditions, but different PH configurations (middle) with their corresponding TEM images (right). Reaction temperature: 150 °C, R_p: 2.25, τ_r: 4 s.

can have similar PL peak positions as thick NPLs, we used TEM imaging to further validate the presence of NPLs versus NCubes in different in-flow synthesized CsPbI$_3$ NC samples (**Figure 5**A). An important factor that must be considered is the delicate nature of small-sized CsPbI$_3$ NCs, where common NC washing methods tend to either destroy the small-sized NCs or alter their morphology due to ligand stripping. Even the use of methyl acetate, the most commonly used antisolvent for purification of CsPbI$_3$ NCs, destroys the smaller NCs during the post-synthesis washing stage, which can be inferred from the disappearance of the lower wavelength PL peaks after washing (see Figure S5, Supporting Information). The detrimental effect of polar antisolvents and harsh NC washing stages on the resultant (smaller) NC populations can negatively impact the accurate understanding of the NC formation mechanism in the reaction vessel. This deficiency highlights the key role of the non-destructive in situ characterization techniques to provide an actual portrayal of the NC population and formation mechanism. Thus, we sought to characterize the NC population both online (in situ absorption and PL) and offline (TEM). Offline characterization requires the separation and purification of the in-flow synthesized CsPbI$_3$ NCs. To preserve a representative population of the different CsPbI$_3$ NC morphologies synthesized in flow, we used hexane as the antisolvent, which proved to be a better alternative to methyl acetate (washing protocol available in the Note S5, Supporting Information) where all lower

PL peaks were preserved post NC washing stage (see Figure S6, Supporting Information). It is worth noting that the antisolvent addition is important to extract the smaller NCs from the crude product mixture, where only centrifugation without any antisolvent addition is not successful in maintaining all CsPbI$_3$ NC populations of the crude mixture (see Figure S6, Supporting Information), as reported by Bonato et al.[31]

Figure 5A presents representative TEM images of CsPbI$_3$ NCs synthesized at four different reaction temperatures and two extreme R_p values (2.25 and 9) at the residence time of 4 s. The residence time of 4 s was selected based on the PL and UV–vis absorption spectra shown in Figure 4, where the PL peak reached its equilibrium position (evident from the similar PL peak position between 4 and 16 s). The spectral data (UV–vis absorption, PL, and PLQY) of the CsPbI$_3$ NC samples presented in Figure 5 along with the TEM images and spectral data of CsPbI$_3$ NCs synthesized at the residence time of 0.6 s are provided in the Supporting Information (see Figures S7,S8, Table S2, Supporting Information). The results shown in Figure 5 reveal a clear morphological difference between CsPbI$_3$ NCs synthesized at R_p of 2.25 versus 9, where the former is dominated by NCubes and the latter by NPLs, that is in agreement with the literature.[20,26,31] In order to better understand the morphological differences of CsPbI$_3$ NCs obtained at different synthesis conditions, we analyzed the TEM images using the following metrics: NC area, circularity, short side length, and
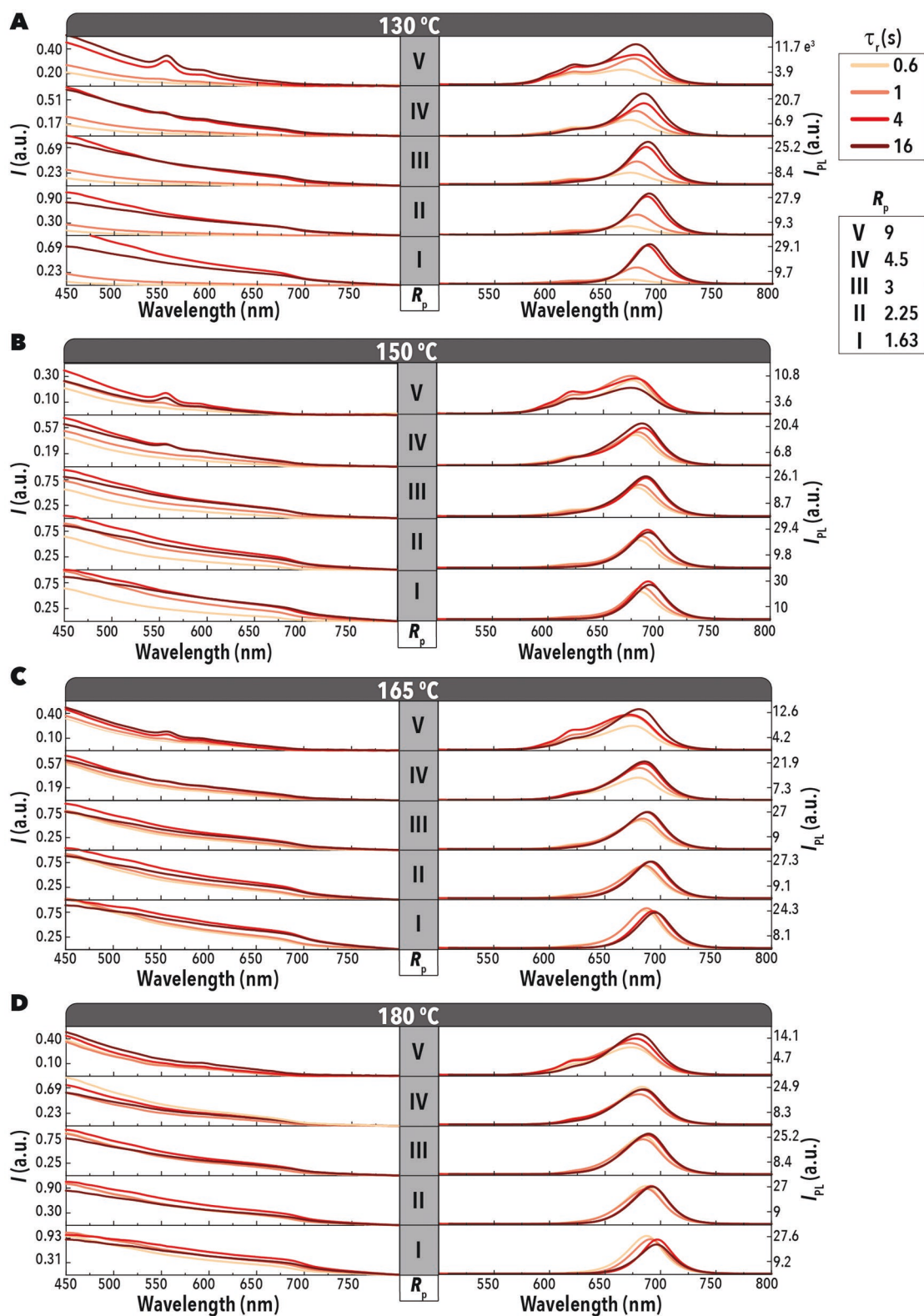
Figure 4. UV–vis absorption (left) and PL spectra (right) of the in-flow synthesized $CsPbI_3$ NCs at different τ_r and R_p values ranging from 0.6 to 16 s and 1.63 to 9, respectively at reaction temperatures of A) 130, B) 150, C) 165, and D) 180 °C. The Y-axes of the absorption (left) and PL (right) plots have the absorbance and arbitrary units, respectively.
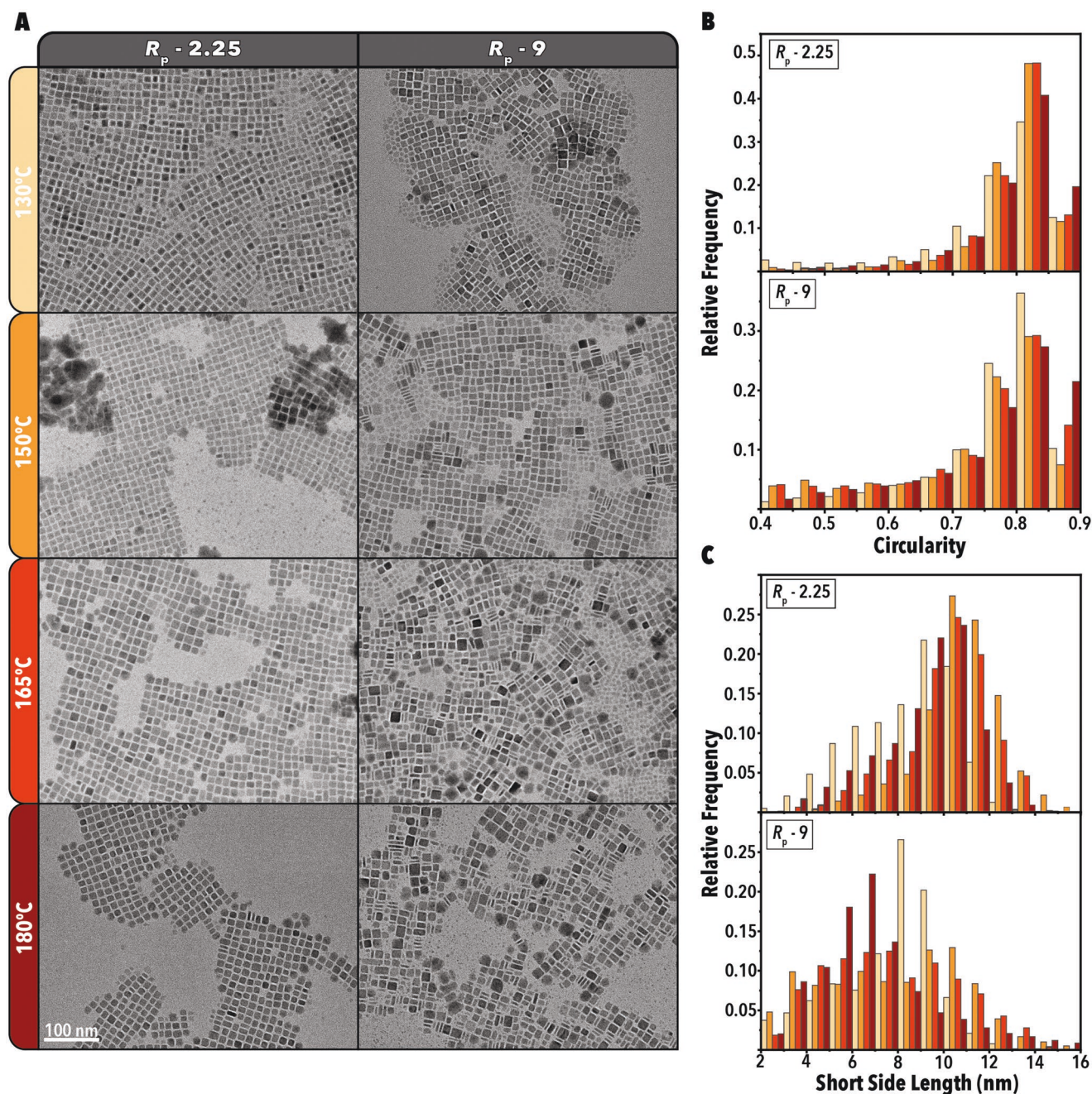
Figure 5. A) TEM images representing the CsPbI$_3$ NC populations at R_p values of 2.25 and 9, and temperatures of 130, 150, 165, and 180 °C at $\tau_r = 4$ s. Histogram plots acquired from the TEM images, showing the relative frequency of the CsPbI$_3$ NCs in terms of B) circularity and C) short side length. The top and bottom panels represent different R_p values (2.25 and 9, respectively). The histogram columns are color-coded, based on the reaction temperature, similar to the color scheme presented in panel (A).

long side length (see Note S8, Supporting Information, for details of the TEM image analysis). Circularity, defined as $\frac{4\pi A}{p^2}$, where A and p are the NC area and perimeter, respectively, can be used as a metric to distinguish between NCubes and NPLs with different edge lengths. Sorting NCs based on their circularity coupled with their area, reveals the dimensional ratio of the NPLs and therefore the length of the short and long side of the NPLs. Histogram plots of the circularity and short side

length of the TEM images shown in Figure 5A are presented in Figure 5B,C, respectively (histograms of the long side length and the full quantitative analysis of Figure S7, Supporting Information are provided in Figures S9,S10, Supporting Information). The first contrasting difference is that the circularity for R_p of 2.25 has a higher overall relative frequency around 0.785 (perfect square) compared to the more spread-out circularity distribution for CsPbI$_3$ NCs synthesized with an R_p of 9 (Figure 5B). This result is complimented with the trend

ADVANCED
SCIENCE NEWS
www.advancedsciencenews.com

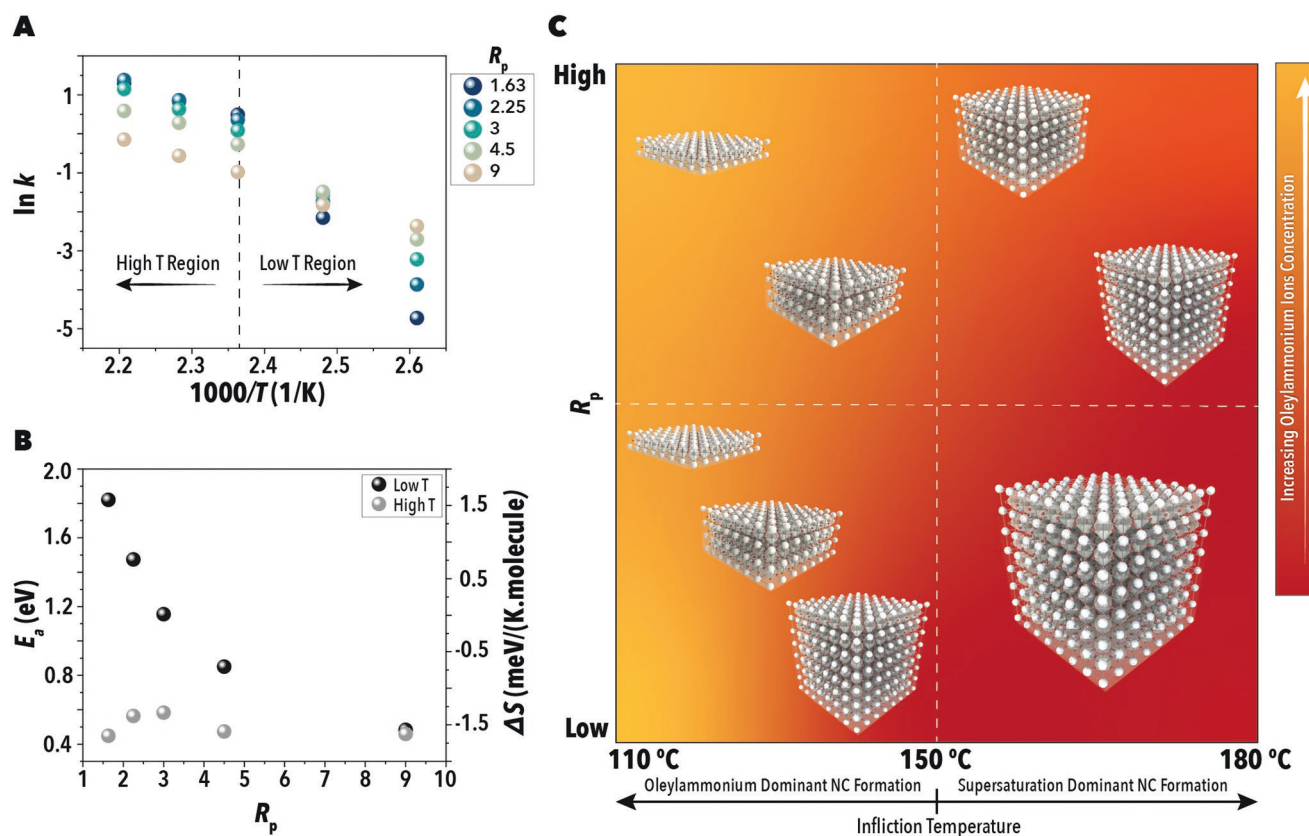**ADVANCED**
FUNCTIONAL
MATERIALS
www.afm-journal.de

Figure 6. A) Arrhenius plot for all R_p values tested in this study, illustrating an inflection point at 150 °C. B) The calculated values of E_a and ΔS around the inflection point for the low (110–150 °C) and high (150–180 °C) temperature regions as a function of R_p. C) A schematic summarizing the factors affecting the formation of $CsPbI_3$ NCs.

shown in Figure 5C, where the majority of the $CsPbI_3$ NCs synthesized at R_p of 2.25 has a short edge length of ≈10–12 nm, that is in agreement with the average size of $CsPbI_3$ NCubes,[1,20] while R_p of 9 exhibited a more spread out NPL population with different thicknesses. $CsPbI_3$ NCs synthesized at a lower residence time of 0.6 s follow a similar pattern at the two extreme values of R_p (see Figure S10, Supporting Information). Further investigation of the $CsPbI_3$ NCs synthesized at different residence times (0.6 s vs 4 s, Figure 5; Figure S10, Supporting Information) reveals that longer reaction times in flow lead to a narrower population distribution and larger NCs.

It is interesting to note that $CsPbI_3$ NC populations with different dominant short side lengths (>6 nm) display similar PL peak wavelengths (Figure 5A; Figures S7,S8, Supporting Information). This finding can be explained by the weakening of the quantum confinement effect that occurs when the size of the NCs approaches the Bohr radius where a change in the NC size has less impact on the emission energy.[1,45] A similar trend has previously been observed for $CsPbI_3$ NPLs, where the NPLs with a minimum monolayer thickness of 10 (corresponding to a short side length of 6 nm) had similar emission energies.[20]

In the next set of experiments, we studied the apparent reaction rate (k)—to better understand the formation of $CsPbI_3$ NCs via the HI synthetic route—through temporal monitoring of the $CsPbI_3$ NCs absorbance at 475 nm (Abs_{475}) as a concentration proxy at different reaction temperatures. It should be noted that τ_r of 16 s was excluded from the k estimation because of the aforementioned size defocusing stage[46] (see Note S9, Figure S11, Table S4, Supporting Information for details of k calculations). Figure S11, Supporting Information shows the temporal concentration evolution of $CsPbI_3$ NCs synthesized at different R_p and reaction temperatures in the flow reactor. The NC growth behavior exhibits increased linearity as R_p increases and temperature decreases. Using the estimated apparent reaction rates, we calculated the activation energy (E_a) of the overall $CsPbI_3$ NC formation reaction using the Arrhenius equation.[47,48] **Figure 6**A presents an interesting behavior for the estimated apparent $CsPbI_3$ NC formation kinetics as a function of the reaction temperature with an inflection point at 150 °C. Non-linear Arrhenius behavior indicates a change in the reaction mechanism or the rate limiting step.[47,49] E_a values, derived from the Arrhenius plots for the two linear regions of the plot shown in Figure 6A (i.e., high temperature zone: 150–180 °C; low temperature zone: 110–150 °C), are presented in Figure 6B. The difference in the formation mechanism of $CsPbI_3$ NCs synthesized at low and high temperature regions is illustrated by the opposing E_a behavior in Figure 6B, where R_p of 1.63 has the highest E_a at low temperatures and the lowest E_a at high temperatures. Next, we coupled the data from the Arrhenius equation with the logarithmic form of the Eyring equation,[50] to gain deeper insights into the entropy (ΔS) and enthalpy (ΔH) of the $CsPbI_3$ NC

**ADVANCED
SCIENCE NEWS**
www.advancedsciencenews.com

**ADVANCED
FUNCTIONAL
MATERIALS**
www.afm-journal.de

formation at different temperatures (see Note S9, Figure S12, Table S5, Supporting Information). The Eyring plot (Figure S12, Supporting Information) illustrates a similar behavior to that of the Arrhenius plot shown in Figure 6A. The calculated values of ΔS for different R_p values are presented in Figure 6B. At low R_p conditions (<4.5), the additional participating Cs^+ ions present in the reaction mixture increases the overall amount of the reactive species relative to higher R_p conditions ($\geq$4.5), resulting in an increase of the overall starting entropy of the system. The low reaction temperatures do not provide sufficient energy to overcome the entropy barrier of $CsPbI_3$ NC formation at low R_p values. This result explains why higher R_p values (4.5 and 9) are more thermodynamically favorable at lower reaction temperatures. The negative ΔS imposes a lower energy cost and reduces the NC formation energy barrier. However, once the provided energy to the flow reactor increases beyond the deflection point (>150 °C), it facilitates overcoming the entropy constraint of the $CsPbI_3$ NC formation.

Before discussing a proposed formation mechanism for colloidal $CsPbI_3$ NCs, two important factors should be considered. The first point involves the role of the surface ligands that are a vital part of the $CsPbI_3$ NC synthesis. Oleylamine (OAm) and OA undergo a reversible exothermic chemical reaction when they are added into the NC precursor solution and the resulting protonation of OAm leads to the formation of oleylammonium ions.[26] Oleylammonium ions have been demonstrated to compete with Cs^+ ions on the $CsPbX_3$ NC surface,[26,51] and inhibit the NC growth on the surface they attach to, thereby resulting in an anisotropic NC growth.[24,26,28,29] Additionally, the presence of oleylammonium and carboxylate species is important for the dissolution of the lead halide salt in the solvent,[26] which explains the inverse solubility behavior that lead halide salts undergo past 180 °C (defining the upper reaction temperature limit used in this study).[5] The other important factor to note is that the formation barrier of an oleylammonium ion layer on the surface of NCs is lower than the formation barrier of $CsPbI_3$.[24]

The formation of $CsPbI_3$ NPLs versus NCubes is determined by the competition between the formation and availability of the oleylammonium ions and $CsPbI_3$ monomers (Figure 6C). At low reaction temperatures, the formation of oleylammonium ions is the dominant phenomena, which significantly increases the probability of oleylammonium ions attaching on the NC surface instead of Cs^+ ions. The rapid oleylammonium attachment to the surface of $CsPbI_3$ NCs prevents the isotropic NC growth, leading to the formation of NPLs. Higher R_p values are thermodynamically favored in this growth regime, due to the lower energy requirements (lower E_a and negative ΔS) associated with these synthesis conditions (Figure 6B). In this regime (low reaction temperatures), low values of R_p incurs a higher energy demand associated with the increased number of available monomers which increases the overall starting entropy of the system. As the reaction temperature increases, the formation rate and concentration of oleylammonium ions decrease due to the exothermic nature of oleylammonium ion formation. The declining availability of the oleylammonium ions in the reaction mixture coupled with the increased energy provided to the system, facilitates monomers overcoming the entropy barrier and decreases the probability of oleylammonium ions

attaching onto the NC surface, resulting in an increased NC growth (thicker NPLs, Figure 6C). As mentioned earlier, the presence of oleylammonium and carboxylate ions is vital for the solubility of PbI_2. Once the reaction temperature passes 150 °C, the reduced solubility of PbI_2 results in a lower supersaturation threshold which increases both the rate and extent of $CsPbI_3$ NC formation in the reaction mixture. The decrease in the supersaturation threshold becomes the dominant phenomena for the formation of $CsPbI_3$ NCs in this regime, where the increased formation rate and energy coupled with the reduced availability of oleylammonium ions promote the formation of thicker NPLs and NCubes at high and low R_p values, respectively. This proposed $CsPbI_3$ NC formation mechanism further explains the size increase and focusing observed as τ_r increases from 0.6 to 4 s. Increasing the reaction time results in an additional flux of energy to the reaction mixture and reduces the available oleylammonium ions in the reaction mixture. The reduced concentration of oleylammonium ions in the solution promotes their desorption from the NC surface which leads to the dissociation of the smaller NCs and the re-initiation of growth on the surface of the larger NCs (i.e., defocusing and Ostwald ripening).

To provide further insights into the proposed $CsPbI_3$ NC formation mechanism, we investigated the effect of available ligands (OA and OAm) present in the PbI_2 precursor on the formation mechanism of $CsPbI_3$ NCs by varying i) the OA to OAm ratio, and ii) the solvent (ODE) to the total ligand ratio. Tuning the OA to OAm ratio controls the concentration of oleylammonium ions, while changing the ODE to ligand ratio affects the monomer supersaturation threshold. Figure S13, Supporting Information shows that increasing the OA to OAm ratio increases the tendency of NPL formation in the $CsPbI_3$ NC population due to an increased OAm protonation (i.e., higher concentration of oleylammonium ions),[26] that is in agreement with our proposed mechanism. Figure S14, Supporting Information provides additional validation to the proposed $CsPbI_3$ NC formation mechanism; higher ODE to ligand ratios (i.e., a lower total available OA and OAm ligands, hence lower concentration of oleylammonium ions) result in a decrease in the monomer supersaturation threshold due to the decrease in the PbI_2 solubility. The lower NC nucleation threshold results in an uncontrolled nucleation event, thereby increasing the polydispersity of the resultant NC population. In contrast, decreasing the ODE to ligand ratio increases the PbI_2 solubility in the reaction mixture, resulting in an increase in the monomer supersaturation threshold, confirmed by no $CsPbI_3$ NC formation until the reaction temperature of 165 °C.

The proposed $CsPbI_3$ NC formation mechanism provides a detailed framework for the flow synthesis of high-quality $CsPbI_3$ NCs with a controlled morphology (NPLs vs NCubes). The synthesis of a monodispersed NCube population of $CsPbI_3$ is readily achieved at the reaction temperature range of 150–165 °C and the R_p values ranging 2.25–3. However, NPL synthesis is preferred at the low temperature range (110–130 °C) and high R_p values (4.5–9), where increasing the temperature in this reaction space results in formation of NPLs with an increased average thickness.

The fast formation kinetics of HI synthesis of $CsPbI_3$ NCs, in addition to challenges associated with their fundamental
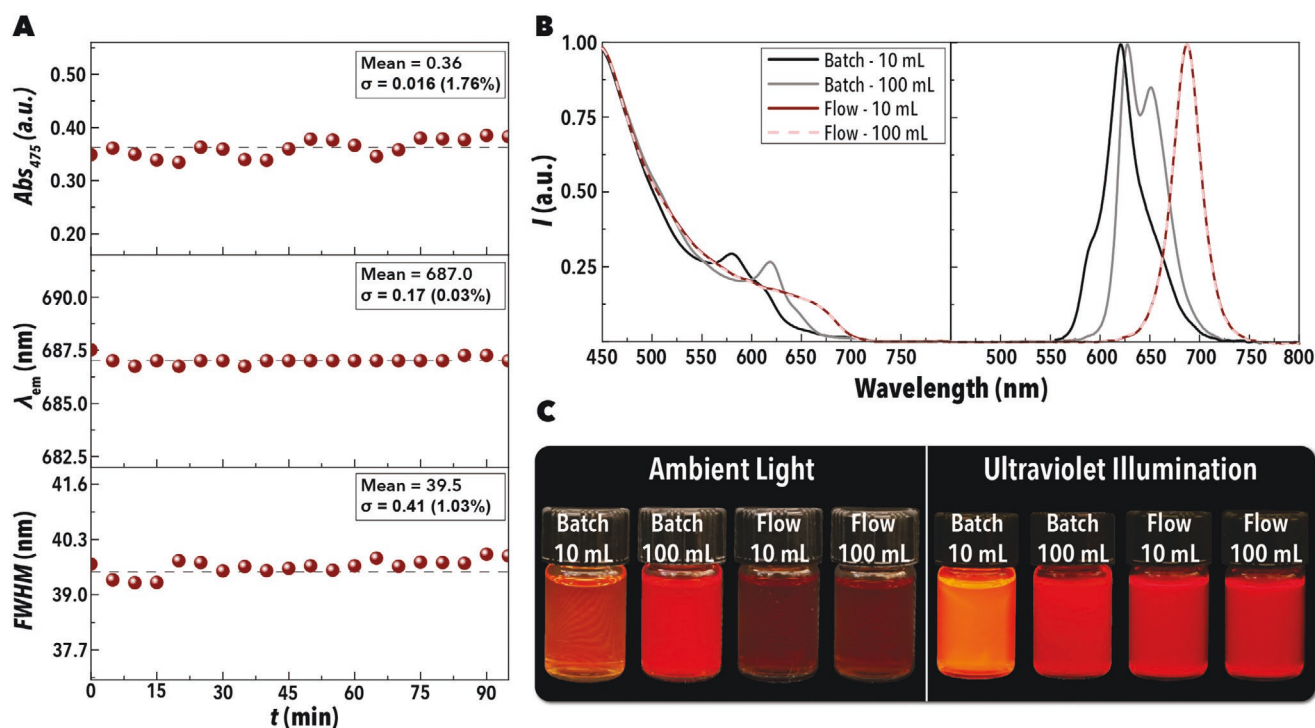
Figure 7. Flow versus batch HI synthesis of CsPbI$_3$ NCs. A) Continuous flow HI synthesis of CsPbI$_3$ NCs over 100 min, illustrating the consistency of absorbance at 475 nm (concentration proxy), peak wavelength (λ_{em}), and full width at half maximum (FWHM) at 5-min intervals. B) Normalized PL and UV–vis absorption spectra of 10 and 100 mL CsPbI$_3$ NC samples synthesized using the HI synthetic route in batch and flow reactors. C) Washed CsPbI$_3$ NC samples synthesized using the flask and flow reactors, under ambient light (left panel) and UV illumination (right panel). Synthesis conditions: [PbI$_2$] = 9 mM, [Cs] = 2 mM, R_p = 2.25, τ_r = 4 s, and the volumetric injection ratio was 1:1. The NC washing method used is described in Note S5, Supporting Information.

mechanistic studies, poses a major limitation on the ability to scale-up their production in a batch reactor (Figure 1). The irre- producible and variable mixing/heat transfer rates as the batch reactor size increases can significantly alter the NC formation kinetics and pathways, thus affecting the size- and morphology- dependent optical and optoelectronic properties of CsPbI$_3$ NCs (Figure 1). In-flow NC synthesis strategies, on the other hand, do not suffer from the same issues as the batch reactors. Increasing the production throughput in a continuous flow reactor can be achieved either through increasing the collection time or scaling out the system by parallelization,[52–54] without altering the mixing and heat transfer dynamics and microre- action environment. It should also be noted that the fast for- mation kinetics of CsPbI$_3$ NCs coupled with the enhanced heat and mass transfer rates of the flow reactors suggest that the optimal NC synthesis protocol and product characteristics, obtained using the developed flow synthesis strategy, cannot be directly transferred to flask-based synthetic methods. To illus- trate this point, a set of experiments was conducted to show- case the difference between the flow- versus flask-based HI syn- thesis of CsPbI$_3$ NCs in terms of the reaction scale and the NC properties. Two target product volumes (10 mL vs 100 mL) were selected to illustrate the role of batch reactor volume on the NC properties. The product output for the HI synthesis conducted in the flow reactor was increased by extending the collection time, where the 10 and 100 mL of the collected CsPbI$_3$ NC solutions corresponded to 10 and 100 min of the continuous

collection, respectively. The product output of the batch reactor was increased by changing the reaction vessel size from a 100 to 250 mL flask size for the 10 and 100 mL synthesis of CsPbI$_3$ NCs, respectively. The reaction conditions selected for these experiments were adopted from the previous flow screening experiments (for details of the synthesis conditions see Note S12, Supporting Information). **Figure 7**A demonstrates the con- sistency and reliability of the HI synthesis of CsPbI$_3$ NCs in the developed modular flow reactor. The continuous flow syn- thesis of CsPbI$_3$ NCs in the flow reactor over 100 min achieved a 0.03%, 1.03%, and 1.76% variation in their λ_{em}, FWHM, and concentration, respectively. The flask-based HI synthesis of CsPbI$_3$ NCs, using the same precursors and synthesis condi- tions used for the continuous flow experiments (Figure 7A), resulted in different NC morphologies and optical properties than the flow reactor, and inconsistent product for different vol- umes of the batch reactors (Figure 7B,C).

The results presented in Figure 7B,C demonstrate the sig- nificant impact of the reaction environment (heat and mass transfer rates) and the batch reactor volume on the colloidal synthesis of CsPbI$_3$ NCs, and thereby their resulting size- and morphology-dependent optical and optoelectronic properties. The PL and UV–vis absorption spectra of the CsPbI$_3$ NCs for the two reaction volumes synthesized using the batch HI syn- thesis technique were vastly different, while the NCs synthe- sized using the in-flow HI synthetic route, developed in this work, were identical for the 10 and 100 mL reaction scales. The

optical properties disparity of $CsPbI_3$ NCs synthesized using the batch and flow synthesis methods (Figure 7B,C), under similar experimental conditions (1:1 volumetric ratio of Cs and PbI_2 precursors), clearly demonstrates that the NC synthesis conditions optimized for the flow synthesis of colloidal NCs with fast formation kinetics under a 1:1 volumetric ratio are not directly interchangeable with batch synthesis methods.

Next, we investigated adoption of a batch-optimized $CsPbI_3$ NC synthesis condition by the developed modular flow chemistry platform. The $CsPbI_3$ NC synthesis protocol used for this test was adopted from the batch-optimized synthesis techniques developed for $CsPbI_3$ NC-based solar cells.[7,17] The volumetric injection ratio of the PbI_2 to Cs precursors in the batch-optimized HI synthesis of $CsPbI_3$ NCs is typically higher than 1:1, due to the poor mixing and heat transfer dynamics of batch reactors at 1:1 volumetric ratios—as evidenced by the results shown in Figure 7B,C. A similar analysis of the batch versus flow synthesis of $CsPbI_3$ NCs to that presented in Figure 7B was conducted for the PbI_2:Cs volumetric ratio of 7.5:1. The results of the batch versus flow synthesis of $CsPbI_3$ NCs using the batch-optimized reaction conditions for two different reaction scales are presented in Figure S15, Supporting Information. As shown in Figure S15, Supporting Information, the in-flow HI synthesis technique resulted in a reliable synthesis of $CsPbI_3$ NCs at two different reaction scales (10 mL vs 100 mL) with optical characteristics identical to the NCs synthesized using a small-scale batch reactor (10 mL). However, increasing the batch reaction vessel size resulted in a blue shift in the UV–vis absorption and PL spectra of $CsPbI_3$ NCs compared to the small-scale batch reactor (Figure S15, Supporting Information). These results demonstrate the compatibility of the developed modular flow reactor with batch-optimized reaction conditions of LHP NCs, thus further promoting flow synthesis strategies as a more versatile approach for fundamental and applied studies of LHP NCs.

The results presented in Figure 7 and Figure S15, Supporting Information demonstrate the unique advantages of the developed fluidic NC synthesizer for the consistent and reliable continuous nanomanufacturing of $CsPbI_3$ NCs for direct utilization in next-generation energy technologies.

3. Conclusion

In summary, we developed and utilized a modular flow synthesis platform integrated with an in situ NC characterization module (UV–vis absorption and PL spectroscopy) for the time- and resource-efficient mechanistic investigations of the formation mechanism and kinetics of colloidal $CsPbI_3$ NCs with a high degree of morphology and emission tunability. The fluidic NC synthesizer allowed us to accurately access early reaction time scales (<1 s) and, for the first time, reveal a complete picture of the dynamic nature of $CsPbI_3$ NC morphologies synthesized via the HI synthetic route. Utilizing the developed flow chemistry route, we rapidly investigated the effects of lead-to-cesium ratio and reaction temperature on the morphology, kinetics, and emission properties of the in-flow synthesized $CsPbI_3$ NCs and proposed a formation mechanism based on the competition between the formation and availability of the oleylammonium ions and $CsPbI_3$ monomers. Low reaction temperatures (<150 °C) are dominated by the formation of oleylammonium ions leading to the formation of NPLs, while high reaction temperatures (>150 °C) result in the formation of NCubes, due to the diminished presence of oleylammonium ions and the decreased $CsPbI_3$ supersaturation threshold.

In addition to the studies of the formation mechanism of colloidal $CsPbI_3$ NCs, we demonstrated reliable and scalable continuous nanomanufacturing (4 s reaction time) of $CsPbI_3$ NCs for next-generation energy technologies, enabled by the in-flow HI synthetic route presented in this work. The developed flow reactor can be readily adapted for nanomanufacturing of other metal halide perovskite NCs beyond $CsPbI_3$, via in-flow HI technique. Further development and adoption of the in-flow HI NC synthesis strategy is expected to significantly accelerate development of optimal formulations and reduce the nanomanufacturing cost of the emerging energy-relevant nanomaterials at a fraction of time and cost of currently utilized manual flask-based experimentation techniques.

4. Experimental Section

Chemicals: All chemicals were used as received. OA (90%), OAm (70%), cesium carbonate (99.9%), lead (II) iodide (99%), and methyl acetate (99%) were purchased from Sigma Aldrich. Hexane and ethanol (70%) were purchased from Fisher Scientific. ODE (90%) and Rhodamine 6G (99%) were purchased from Acros Organics. PFO (HT-200) was purchased from Galden.

$CsPbI_3$ NC Synthesis: Colloidal synthesis of $CsPbI_3$ NCs was adopted from Protesescu et al.[1] with minor modifications for adaptation with flow synthesis. Specifically, the precursor concentrations used in this study were reduced and modified to: i) allow for a volumetric injection ratio of 1:1 in the flow reactor, ii) achieve a cesium carbonate concentration that allowed the salt to remain in solution at room temperature, and iii) ensure that the $CsPbI_3$ product concentration did not saturate the in situ measured UV–vis absorption spectra across the different experimental conditions.

Lead Iodide Precursor Preparation: PbI_2 was prepared with a concentration of 9 mM for all experimental conditions tested in this study. Briefly, for the preparation of 48 mL of the PbI_2 precursor, a mixture of ODE (40 mL), OA (4 mL), OAm (4 mL), and PbI_2 (199 mg) were loaded into a 100 mL 3-neck round bottom flask. The solution was dried under vacuum for 1 h at 120 °C and then flushed with N_2. The PbI_2 precursor was then cooled down to room temperature, loaded into a 50 mL stainless steel syringe (KD scientific), and connected to the flow synthesis platform.

Cesium Precursor Preparation: Cs precursor was prepared with a concentration of 3 mM. As mentioned in the main manuscript, the lead-to-cesium ratio (R_p) was changed to the desired synthesis condition by varying the Cs precursor concentration in flow with a solution of ODE and OA (with a volumetric ratio of 16:1). Briefly, for the preparation of 20 mL of the Cs precursor, a mixture of ODE (18.824 mL), OA (1.176 mL), and cesium carbonate (19.55 mg) were loaded into a 100 mL 3-neck round bottom flask. The solution was dried under vacuum for 1 h at 120 °C and then flushed with N_2. The prepared Cs precursor was then cooled down to room temperature, loaded into a 20 mL stainless steel syringe (KD scientific), and connected to the flow synthesis platform.

Flow Screening Conditions: The main flow screening experiments of this work revolved around $CsPbI_3$ HI reactions and the parameters explored were: temperature (110, 130, 150, 165, and 180 °C), R_p (1.63, 2.25, 3, 4.5, and 9), and τ_r (0.6, 1, 4, and 16 s). It is worth to note that the desired R_p was attained by keeping the concentration of the lead iodide precursor constant while changing the concentration of the Cs precursor, and the desired τ_r values were varied by changing the reactor length. τ_r values of

0.6 and 1 s were chosen to access early timescales, 4 s as the time that was reported for the completion of $CsPbI_3$ synthesis.[35] 16 s was chosen to observe the effect of extended reaction times on $CsPbI_3$ NCs.

Conflict of Interest

The authors declare no conflict of interest.

Data Availability Statement

The data that support the findings of this study are available from the corresponding author upon reasonable request.

[1] L. Protesescu, S. Yakunin, M. I. Bodnarchuk, F. Krieg, R. Caputo, C. H. Hendon, R. X. Yang, A. Walsh, M. V. Kovalenko, *Nano Lett.* **2015**, *15*, 3692.

[2] J. Shamsi, A. S. Urban, M. Imran, L. De Trizio, L. Manna, *Chem. Rev.* **2019**, *119*, 3296.

[3] A. Dey, J. Ye, A. De, E. Debroye, S. K. Ha, E. Bladt, A. S. Kshirsagar, Z. Wang, J. Yin, Y. Wang, *ACS Nano* **2021**, *15*, 10775.

[4] K. Abdel-Latif, F. Bateni, S. Crouse, M. Abolhasani, *Matter* **2020**, *3*, 1053.

[5] A. Swarnkar, A. R. Marshall, E. M. Sanehira, B. D. Chernomordik, D. T. Moore, J. A. Christians, T. Chakrabarti, J. M. Luther, *Science.* **2016**, *354*, 92.

[6] J. Yuan, A. Hazarika, Q. Zhao, X. Ling, T. Moot, W. Ma, J. M. Luther, *Joule* **2020**, *4*, 1160.

[7] Y. Wang, J. Yuan, X. Zhang, X. Ling, B. W. Larson, Q. Zhao, Y. Yang, Y. Shi, J. M. Luther, W. Ma, *Adv. Mater.* **2020**, *32*, 2000449.

[8] J. Yuan, X. Ling, D. Yang, F. Li, S. Zhou, J. Shi, Y. Qian, J. Hu, Y. Sun, Y. Yang, *Joule* **2018**, *2*, 2450.

[9] A. R. Kirmani, J. M. Luther, M. Abolhasani, A. Amassian, *ACS Energy Lett.* **2020**, *5*, 3069.

[10] X. Wang, Z. Bao, Y.-C. Chang, R.-S. Liu, *ACS Energy Lett.* **2020**, *5*, 3374.

[11] J. Song, J. Li, X. Li, L. Xu, Y. Dong, H. Zeng, *Adv. Mater.* **2015**, *27*, 7162.

[12] X. Zhu, Y. Lin, Y. Sun, M. C. Beard, Y. Yan, *J. Am. Chem. Soc.* **2019**, *141*, 733.

[13] J. Yuan, H. Liu, S. Wang, X. Li, *Nanoscale* **2021**, *13*, 10281.

[14] X. Ling, S. Zhou, J. Yuan, J. Shi, Y. Qian, B. W. Larson, Q. Zhao, C. Qin, F. Li, G. Shi, *Adv. Energy Mater.* **2019**, *9*, 1900721.

[15] K. Chen, W. Jin, Y. Zhang, T. Yang, P. Reiss, Q. Zhong, U. Bach, Q. Li, Y. Wang, H. Zhang, *J. Am. Chem. Soc.* **2020**, *142*, 3775.

[16] Q. Zhao, A. Hazarika, X. Chen, S. P. Harvey, B. W. Larson, G. R. Teeter, J. Liu, T. Song, C. Xiao, L. Shaw, M. Zhang, G. Li, M. C. Beard, J. M. Luther, *Nat. Commun.* **2019**, *10*, 2842.

[17] F. Li, S. Zhou, J. Yuan, C. Qin, Y. Yang, J. Shi, X. Ling, Y. Li, W. Ma, *ACS Energy Lett.* **2019**, *4*, 2571.

[18] Y. Bekenstein, B. A. Koscher, S. W. Eaton, P. Yang, A. P. Alivisatos, *J. Am. Chem. Soc.* **2015**, *137*, 16008.

[19] M. C. Weidman, M. Seitz, S. D. Stranks, W. A. Tisdale, *ACS Nano* **2016**, *10*, 7830.

[20] Y. Tong, E. Bladt, M. F. Aygüler, A. Manzi, K. Z. Milowska, V. A. Hintermayr, P. Docampo, S. Bals, A. S. Urban, L. Polavarapu, *Angew. Chem., Int. Ed.* **2016**, *55*, 13887.

[21] H. Huang, Y. Li, Y. Tong, E. Yao, M. W. Feil, A. F. Richter, M. Döblinger, A. L. Rogach, J. Feldmann, L. Polavarapu, *Angew. Chem., Int. Ed.* **2019**, *58*, 16558.

[22] S. K. Ha, C. M. Mauck, W. A. Tisdale, *Chem. Mater.* **2019**, *31*, 2486.

[23] Y. Zhang, C. Wang, Z. Deng, *Chem. Commun.* **2018**, *54*, 4021.

[24] V. M. Burlakov, Y. Hassan, M. Danaie, H. J. Snaith, A. Goriely, *J. Phys. Chem. Lett.* **2020**, *11*, 6535.

[25] Q. A. Akkerman, S. G. Motti, A. R. Srimath Kandada, E. Mosconi, V. D'Innocenzo, G. Bertoni, S. Marras, B. A. Kamino, L. Miranda, F. De Angelis, *J. Am. Chem. Soc.* **2016**, *138*, 1010.

[26] G. Almeida, L. Goldoni, Q. Akkerman, Z. Dang, A. H. Khan, S. Marras, I. Moreels, L. Manna, *ACS Nano* **2018**, *12*, 1704.

[27] X. Sheng, G. Chen, C. Wang, W. Wang, J. Hui, Q. Zhang, K. Yu, W. Wei, M. Yi, M. Zhang, *Adv. Funct. Mater.* **2018**, *28*, 1800283.

[28] M. Chen, H. Hu, N. Yao, X. Yuan, Q. Zhong, M. Cao, Y. Xu, Q. Zhang, *J. Mater. Chem. C* **2019**, *7*, 14493.

[29] A. Pan, B. He, X. Fan, Z. Liu, J. J. Urban, A. P. Alivisatos, L. He, Y. Liu, *ACS Nano* **2016**, *10*, 7943.

[30] B. A. Koscher, N. D. Bronstein, J. H. Olshansky, Y. Bekenstein, A. P. Alivisatos, *J. Am. Chem. Soc.* **2016**, *138*, 12065.

[31] L. G. Bonato, R. F. Moral, G. Nagamine, A. Alo, J. C. Germino, D. S. da Silva, D. B. Almeida, L. F. Zagonel, F. Galembeck, L. A. Padilha, *Angew. Chem., Int. Ed.* **2020**, *59*, 11501.

[32] N. T. K. Thanh, N. Maclean, S. Mahiddine, *Chem. Rev.* **2014**, *114*, 7610.

[33] T. Sugimoto, *Monodispersed Particles*, Elsevier, Amsterdam **2019**.

[34] A. Riedinger, F. D. Ott, A. Mule, S. Mazzotti, P. N. Knüsel, S. J. P. Kress, F. Prins, S. C. Erwin, D. J. Norris, *Nat. Mater.* **2017**, *16*, 743.

[35] I. Lignos, S. Stavrakis, G. Nedelcu, L. Protesescu, A. J. deMello, M. V. Kovalenko, *Nano Lett.* **2016**, *16*, 1869.

[36] I. Lignos, R. M. Maceiczyk, M. V. Kovalenko, S. Stavrakis, *Chem. Mater.* **2020**, *32*, 27.

[37] S.-M. Kang, B. Park, G. S. R. Raju, S. Baek, S. K. Hussain, C. H. Kwak, Y.-K. Han, J. S. Yu, S.-W. Kim, Y. S. Huh, *Chem. Eng. J.* **2020**, *384*, 123316.

[38] S. Li, R. W. Baker, I. Lignos, Z. Yang, S. Stavrakis, P. D. Howes, A. J. deMello, *Mol. Syst. Des. Eng.* **2020**, *5*, 1118.

[39] Z. Zhang, Y. Liu, C. Geng, S. Shi, X. Zhang, W. Bi, S. Xu, *Nanoscale* **2019**, *11*, 18790.

[40] K. Abdel-Latif, R. W. Epps, F. Bateni, S. Han, K. G. Reyes, M. Abolhasani, *Adv. Intell. Syst.* **2021**, *3*, 2000245.

[41] F. Bateni, R. W. Epps, K. Abdel-latif, R. Dargis, S. Han, A. A. Volk, M. Ramezani, T. Cai, O. Chen, M. Abolhasani, *Matter* **2021**, *4*, 2429.

[42] A. M. Nightingale, T. W. Phillips, J. H. Bannock, J. C. De Mello, *Nat. Commun.* **2014**, *5*, 3777.

[43] R. W. Epps, K. C. Felton, C. W. Coley, M. Abolhasani, *Lab Chip* **2017**, *17*, 4040.

[44] K. Abdel-Latif, R. W. Epps, C. B. Kerr, C. M. Papa, F. N. Castellano, M. Abolhasani, *Adv. Funct. Mater.* **2019**, *29*, 1900712.

[45] S. M. Bhagyaraj, O. S. Oluwafemi, N. Kalarikkal, S. Thomas, *Synthesis of Inorganic Nanomaterials Advances and Key Technologies*, Elsevier, Amsterdam **2018**.

[46] M. Koolyk, D. Amgar, S. Aharon, L. Etgar, *Nanoscale* **2016**, *8*, 6403.

[47] W. Wang, C. J. Roberts, *AAPS J.* **2013**, *15*, 840.

[48] A. Hazarika, Q. Zhao, E. A. Gaulding, J. A. Christians, B. Dou, A. R. Marshall, T. Moot, J. J. Berry, J. C. Johnson, J. M. Luther, *ACS Nano* **2018**, *12*, 10327.

[49] K. C. Waterman, R. C. Adami, *Int. J. Pharm.* **2005**, *293*, 101.

[50] H. Eyring, *J. Chem. Phys.* **1935**, *3*, 107.

[51] M. I. Bodnarchuk, S. C. Boehme, S. ten Brinck, C. Bernasconi, Y. Shynkarenko, F. Krieg, R. Widmer, B. Aeschlimann, D. Günther, M. V. Kovalenko, I. Infante, *ACS Energy Lett.* **2018**, *4*, 63.

[52] J. Zhang, K. Wang, A. R. Teixeira, K. F. Jensen, G. Luo, *Annu. Rev. Chem. Biomol. Eng.* **2017**, *8*, 285.

[53] C. T. Riche, E. J. Roberts, M. Gupta, R. L. Brutchey, N. Malmstadt, *Nat. Commun.* **2016**, *7*, 10780.

[54] L. Wang, L. R. Karadaghi, R. L. Brutchey, N. Malmstadt, *Chem. Commun.* **2020**, *56*, 3745.